Impact of Shape and Pore Size of Mesoporous Silica Nanoparticles on Serum Protein Adsorption and RBCs Hemolysis

Zhifang Ma,[†,‡] Jing Bai,[†] Yichen Wang,[†,‡] and Xiue Jiang*,[†]

[†]State Key Laboratory of Electroanalytical Chemistry, Changchun Institute of Applied Chemistry, Chinese Academy of Science, Changchun, Jilin, 130022, People's Republic of China

[‡]University of Chinese Academy of Sciences, Beijing, 100049, People's Republic of China

Ⓢ *Supporting Information*

ABSTRACT: With the rapid development of nanotechnology, mesoporous silica nanoparticles (MSNs) with numerous forms and structures have been synthesized and extensively applied in biomedicine in the past decades. However, our knowledge about the biocompatibility of the developed MSNs has not matched their development. Therefore, in this work, we have synthesized sphere-shaped MSNs with different pore scales (s-SPs and l-SPs) and rod-shape (RPs-3) MSNs to evaluate the influence of the morphology and pore size on their interaction with serum proteins and red blood cells (RBCs). The adsorption of human albumin (HSA), globulin (HGG), and fibrinogen (HSF) onto different kinds of MSNs has been analyzed by pseudo second-order kinetic model, and the conformational changes of the adsorbed proteins have been studied by FTIR spectroscopy. We find that the conformation of absorbed HSA and HSF, while not HGG, will be affected by the pore size and morphology of the MSNs. The conformational changes of the adsorbed proteins will further affect their saturated adsorption capacity. However, the initial adsorption rate is only determined by the property of MSNs and proteins. Additional hemolysis assay shows that the pore size and morphology of the MSNs will also affect their hemolytic activity in RBCs which will be extremely depressed by the formation of protein corona. These systematic studies will provide an overall understanding in the blood compatibility of MSNs as well as useful guidelines for fabrication of blood-compatible nanomaterials.

KEYWORDS: MSNs, serum proteins, adsorption kinetics, conformational changes, RBCs hemolysis
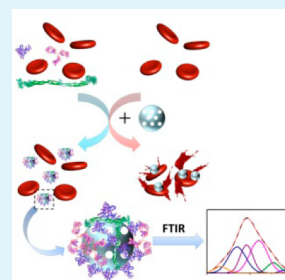
1. INTRODUCTION

Engineered nanoparticles have rapidly expanded in different areas of industry, technology, and medicine in the past decades, which increases the chance of human exposure to the nanoparticles in our daily life. The respiratory system, skin, and gastrointestinal tract are the usual routes that nanoparticles enter into the body in the daily exposure, and intravenous injection is the most common entrance way of most nanoparticles applied in biomedicine. In all cases, nanoparticles will reach the bloodstream and interact with blood components. Interaction between nanomaterials and serum proteins may alter the protein conformation, orientation and expose so-called hidden epitopes, eventually leading to functional disturbing.[1,2] The adsorbed protein will further modify the surface of nanoparticles and constitute a major element of the biological identity on the surface of nanoparticles.[3,4] Interaction of nanoparticles with red blood cells (RBCs) often causes RBC hemolysis.[5−8] RBCs also change the responses of human body defense system to the adsorbed nanoparticles, which either improve the particles in vivo circulation lifetime[9] or reduce the susceptibility of particles to macrophages.[10] To clarify the interaction between nanoparticles and proteins as well as RBCs may have guiding significance in the design and engineering of nanoparticles with improved biocompatibility. Therefore, the evaluation of blood compatibility is the basis for the reduction of nanotoxicity and the improvement of therapeutic applications of nanoparticles.

With the booming development of nanotechnology in the past decades, MSNs stand out among the recent nanotechnology-derived candidates, for their biomedical applications, such as bio-imaging, bio-sensing, bio-catalysis, and drug delivery.[11−13] They possess various unique physicochemical properties such as, for instance, easy synthesis, controllable particles scale and different morphologies ranging from spheres to rods, uniform cylindrical mesopores, high surface areas, and available surface modification.[14,15] Therefore, MSNs have been extensively investigated as robust platforms for different biological or medical applications. However, our knowledge about the blood compatibility of MSNs does not match with numerous forms and structures of synthesized MSNs as intravascular drug carriers. Till now, there are only a few reports investigating the biocompatibility of MSNs on RBCs.[16−22] Depending on the type of MSNs studied to date, quite different conclusions have been drawn. Lin and co-workers studied the impacts of MSNs size, pore ordering, and pore integrity on hemolytic activity and found that the hemolytic activity was diminished to a certain degree with

the increase of the size of MSNs from 25 to 225 nm.[18] MSNs showed lower hemolytic activity than their nonporous counterparts of similar size.[18] In contrast, Zhao and co-workers found that small MSNs with a diameter of 100 nm reduced the hemolytic activity than big MSNs (∼600 nm).[16] Yu and co-workers found that MSNs showed higher hemolytic activity than their nonporous counterparts of similar size.[17] Madhura Jogkekar and co-workers reported that spherical nanoparticles exhibit lower hemolytic activity (less than 2%) than their tubular counterparts,[20] contrasting to the reported trend by Yu and co-workers[19] about the effect of morphology of MSNs on RBCs hemolysis, although they explained the difference could be attributed to lower surface charge and the difference in synthetic methodology.[20] More recently, it was found that the hemolytic activity of bare MSNs can be effectively reduced by surface modification.[21,22] Nevertheless, these disagreeing conclusions stress the challenge for studying the interaction of MSNs with RBCs. It is even surprising that there are very few studies investigating the biocompatibility of MSNs on serum proteins such as, for instance, the effect of MSNs on protein structure, although some researchers studied the impact of surface modification on protein adsorption capacity.[21,22] It is clear that any potential nanotoxicity effect of these MSNs should be evaluated before their therapeutic applications.

Studies showed that the same nanomaterial could lead to very different biological responses, when exposed to cells in the presence of serum proteins or not.[23] Bare silica nanoparticles exposed to cells have a stronger adhesion to the cell membrane and higher internalization efficiency, in comparison with when a preformed corona is present on their surfaces.[23] Binding of blood proteins to carbon nanotubes could reduce the cytotoxicity.[24] A deep-going understanding of the biological effects of nanoparticles requires inspecting the kinetic process and equilibrium state of blood components binding to nanoparticles. Although lots of studies have defined the biocompatibility of nanoparticles by observing their hemolysis, it has to be re-evaluated by considering the effects of serum proteins; for instance, the formation of plasma corona can significantly inhibit the hemolytic activity of MSNs with different morphologies[20] and silica nanoparticles with different sizes. J. Shia et al. concluded that small size and large external surface area were generally observed for hemolytic particles and the reduction of silanol groups and electrostatic/steric repulsion between the particles and RBC reduces hemolytic activities of particles.[25] In this work, sphere and rod-shaped MSNs were synthesized to evaluate the influence of morphology on serum proteins adsorption including adsorption kinetics and conformational changes by using albumin, γ-globulin, and fibrinogen as model proteins, and RBCs hemolysis, respectively. To compare the effect of the pore size, sphere-shaped MSNs with different pore sizes were synthesized and evaluated. This is the first work that studies the influence of MSNs morphology and pore size on protein adsorption property and the impact of pore size on RBCs hemolysis. Furthermore, we also studied the hemolytic activity of different MSNs in the presence of serum proteins. Our study will provide an overall understanding in the blood compatibility of MSNs and have guiding significance in the fabrication of blood-compatible nanomaterials.

2. EXPERIMENTAL SECTION

Chemicals. Cetyltrimethylammonium bromide (CTAB, 99%), ammonium hydroxide (NH₄OH, 28−30 wt % as NH₃), and tetraethyl orthosilicate (TEOS, 98%) were obtained from Beijing Chemical Reagents Company (China). A BCA protein assay kit was purchased from Beijing Bioteke Corporation (China). Calcium- and magnesium-free Dulbecco's phosphate-buffered saline (PBS) was obtained from Invitrogen. Human serum albumin (HSA) (A1653), human γ-globulin (G5385), and human fibrinogen (F-4883) were purchased from Sigma Chemical Company. The deionized (D.I.) water was generated using a Millipore Milli-Q system (Billerica, MA). All chemicals were used without additional purification.

Preparation of MSNs. The MSNs were prepared using an ammonia base-catalyzed method under a highly diluted silica source and low surfactant concentration conditions.[17,26] The particle shape was controlled by adjusting the ammonia concentration, TEOS volume added, and CTAB concentration. For preparation of sphere-shaped particles (s-SPs), the molar ratio of the reaction mixture was 0.1 (CTAB):1000 (H₂O):5 (NH₃·H₂O):0.7 (TEOS), whereas the molar ratio of the reaction mixture for preparation of rod-shaped particles was adjusted to 0.4 (CTAB):1000 (H₂O):10 (NH₃·H₂O):1.4 (TEOS). Typically, in the synthesis of s-SPs, 0.3 g of CTAB was dissolved in 150 mL of 0.28 M ammonium hydroxide solution at room temperature (25 °C), stirring for 1 h. Then, 1310 μL of 5.8 mM TEOS was added to the solution dropwise under vigorous stirring, then the solution was continuously stirred for 3 h at 25 °C. The as-synthesized nanoparticles were collected by centrifugation and washed with water and ethanol for three times, respectively, and then dried under high vacuum at 60 °C for 8 h. The powder was calcined at 550 °C for 6 h to remove any remaining organic species. Alternatively, prior to calcination, 1 g of the surfactant-containing s-SPs powder was added to 60 mL of a water/ethanol (50/50; v/v) solution including 2.25 g of benzene as a swelling agent. Then, the mixture was sealed and placed in an oven at 100 °C for 1 day without stirring. The obtained complex was centrifuged, washed, dried, and calcined with the identical conditions as the preparation of the s-SPs to get large pore size sphere-shaped particles (l-SPs).[27,28] The as-prepared MSNs were characterized by transmission electron microscopy (TEM) measurements on a HITACHI H-8100EM microscope (Hitachi, Japan). Nitrogen adsorption−desorption measurements were made on an ASAP 2020−Physisorption Analyzer (Micromeritics, USA). The specific surface area was calculated using Brunauer−Emmett−Teller (BET) equation at $P/P_0 < 0.3$. The pore size distribution was calculated from the branch of the adsorption isotherm using a Barrett−Joyner−Halenda (BJH) method.

Adsorption of Serum Proteins onto MSNs. Adsorption of three major human serum proteins, HSA, HGG, and HSF, onto MSNs were measured at pH 7.4 PBS. In the assessment of adsorption kinetics, 400 μL of an HSA (10 mg/mL), HGG (6.25 mg/mL), and HSF (1 mg/mL) PBS solution were added, respectively, into 600 μL of 0.83 mg/mL MSNs PBS solution and the mixtures were incubated at 37 °C for 5, 10, 20, 40, and 80 min, respectively. Then the mixture was centrifuged at 10,016g for 3 min. The supernatant was carefully removed from the centrifugal tube and the concentration of protein in the supernatant was determined using BCA assay kits. The amount of adsorbed protein was calculated from the differences between the initial and the equilibrated concentrations.

Attenuated Total Reflectance Fourier Transform Infrared Spectroscopy (ATR-FTIR). Alternatively, after proteins and MSNs were incubated for 80 min, 10 μL of the mixture was spread uniformly on the surface of a one-reflection horizontal ATR accessory with a silicon crystal. The mixture was then evaporated at room temperature under airflow for 10 min before ATR-FTIR absorption spectra were measured. 256 scans were collected for each spectrum with a spectrum resolution of 4 cm⁻¹ and All ATR-FTIR absorption spectra were recorded with a spectrometer (IFS 66 s/v, Bruker, Ettlingen, Germany) equipped with a liquid-nitrogen-cooled MCT detector. The spectrum was corrected by subtraction of absorption bands of PBS and vaporized water in the atmosphere. To enhance spectral resolution, some spectra were decomposed to separate overlapping peaks by Gaussian curve-fitting analysis, which was carried out by using the OPUS 5.0 software in the interactive mode. The positions of the component bands determined by the second-derivative peaks were set
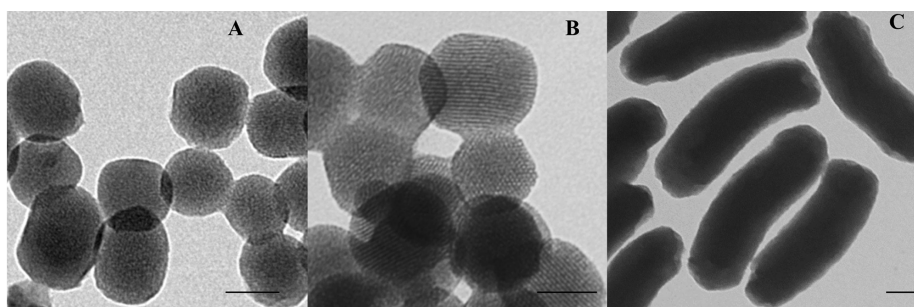
Figure 1. TEM images of (A) small pore size sphere-shaped MSNs (*s*-SPs), (B) large pore size sphere-shaped MSNs (*l*-SPs), (C) rod-shaped MSNs (RPs). Scale bars in A−C = 50 nm.

as the initial input parameters. The program iterated to achieve the best Gaussian-shaped curves which fit the original spectra. The best fit was determined by the root-mean-square (rms) of the difference between the original spectrum and the sum of all individual-resolved bands. The relative amount of different compositions was calculated from the integrated areas of the component bands.

Hemolysis Assay. Human blood samples were freshly obtained from multiple healthy adult volunteers in the Affiliated Hospital of Northeast Normal University (St. Renmin, Changchun). Whole blood was centrifuged at 10,016*g* for 3 min to remove the plasma, buffy coat, and top layer of cells. Then, 2 mL of blood sample was added to 4 mL of sterile PBS, and RBCs were isolated by centrifugation at 10,016*g* for 3 min. The RBCs were further washed five times with 20 mL of PBS solution. The purified blood was diluted to 20 mL PBS. Typically, for hemolysis measurement, 0.2 mL of the diluted RBCs suspension taken from the 20 mL stock solution was added to 0.8 mL of 625 μg/mL MSNs suspension in PBS. The suspension was placed in the thermostatic oscillator (THZ-98C, Shanghai Yiheng, China) and vigorously shaken (200 rpm/min) at 37 °C for different times, followed by centrifugation at 10,016*g* for 3 min. A 200 μL amount of supernatant from the sample tube was transferred to a 96-wellplate. The absorbance value of the hemoglobin at 577 nm was measured with the reference wavelength of 655 nm using a Synergy HT Multimode Microplate Reader (Bio-Tek Instruments, Inc., Winooski, VT, USA). Meanwhile, a 0.2 mL amount of diluted RBC suspension incubated with 0.8 mL of PBS or 0.8 mL of water was used as the negative or positive control, respectively. The percent of hemolysis was calculated as follows: Hemolysis% = [(sample absorbance − negative control)/(positive control − negative control)] × 100%.

3. RESULTS AND DISCUSSION

Fabrication and Characterization of Different MSNs. We prepared a series of MSNs with varying pore sizes and shapes by a cocondensation method under diluted TEOS and low surfactant concentration conditions with aqueous ammonia as a base catalyst.[17,26] RPs-3 with an aspect ratio of ∼3 (RPs-3) was fabricated by controlling the concentration of reaction reagents and stirring rate in this reaction. The width of rod-shaped MSNs was controlled by varying the concentration of ammonia, and the length was controlled by increasing the concentration of TEOS, CTAB, and ammonia, as well as reducing the stirring speed. The pore expansion is through the introduction of a swelling agent into the structure-directing template in the preparation step so as to ensure *s*-SPs and *l*-SPs have the same diameter.[27,28] The as-prepared MSNs were calcined at 550 °C for 6 h to remove the surfactant. The size and morphology of the synthesized MSNs were characterized by TEM measurements. Typical TEM images are shown in Figure 1. It is evident that the two kinds of sphere-shaped MSNs have similar diameters of about 70 nm. Rod-shaped MSNs have a similar diameter to that of sphere-shaped MSNs, and the aspect ratio is about 3. The surface area and the pore

size of the MSNs were characterized by nitrogen adsorption−desorption analysis. All physicochemical properties of the MSNs were compiled in Table 1. The *s*-SPs and the *l*-SPs have

Table 1. Physicochemical Characteristics of the Three Types of MSNs

	average particles diameter (nm)	pore size (nm)	surface area (m²/g)
s-SPs	67 ± 3	2.2	1255.6
l-SPs	68 ± 4	3.0	947.21
RPs-3	(107 ± 8) × (343 ± 16)	2.2	1140.8

different pore sizes (2.2 and 3 nm) and surface areas (1255.6 m²/g and 947.2 m²/g), whereas the RPs-3 have nearly the same pore size (2.2 nm) and surface area (1140.8 m²/g) as the *s*-SPs.

Effect of Pore Size and Shape of MSNs on Protein Adsorption. Serum protein adsorption is the first event once nanomaterials enter into biological fluid; therefore, it is important to study the adsorption of serum proteins onto the MSNs due to their extensive applications in nanomedicine. Adsorption of proteins is related to many factors, such as physicochemical properties of nanomaterials and nature of proteins. To evaluate the effect of physicochemical properties, we prepared sphere-shaped MSNs with smaller (*s*-SPs) and bigger (*l*-SPs) pores and rod-shaped MSNs (RPs-3) with the same pore size as the *s*-SPs. To evaluate the effect of protein nature, we selected HSA, HGG, and HSF, three major proteins in serum, as model proteins. Overall, the adsorption of these three proteins onto the three MSNs had similar tendency, which was especially rapid within the initial 5 min, and thereafter tended to increase slowly till reaching equilibrium (Figure 2). The detail adsorption mechanism of HSA, HGG, and HSF onto the *s*-SPs, *l*-SPs, and RPs-3 can be evaluated by pseudo-second-order kinetic model, which is applicable to describe the behavior over the whole range of adsorption. A pseudo-second-order equation can be expressed as follows:[29]

$$\frac{dq_t}{dt} = k_2(q_e - q_t)^2$$

(eq 1)

where k_2 (mg^{-1}·m^2·min^{-1}) is the rate constant, q_e (mg·m^{-2}) is the saturated adsorption capacity, and q_t (mg·m^{-2}) is the adsorption amount at time t (min). After definite integration by applying the boundary conditions $q_t = 0$ at $t = 0$ and $q_t = q_t$ at $t = t$, the rearranged eq eq 1 becomes the following:

$$\frac{t}{q_t} = \frac{1}{k_2 q_e^2} + \frac{1}{q_e}t$$
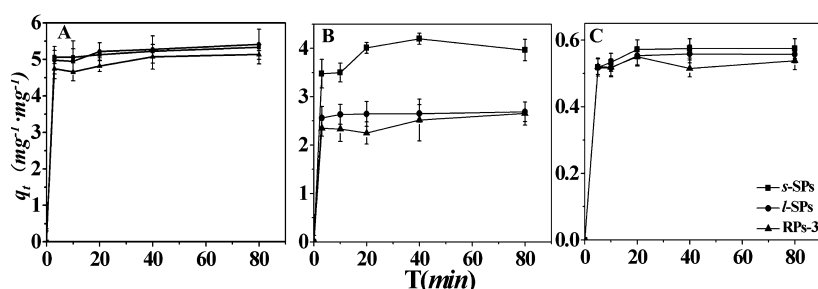
(eq 2)

Figure 2. Adsorption amount of three serum proteins (A) HSA, (B) HGG, (C) HSF onto different MSNs at 37 °C in pH 7.4 PBS, plotted as a function of time. The value was obtained from two or three experiments; error bars indicate standard deviations from the mean.
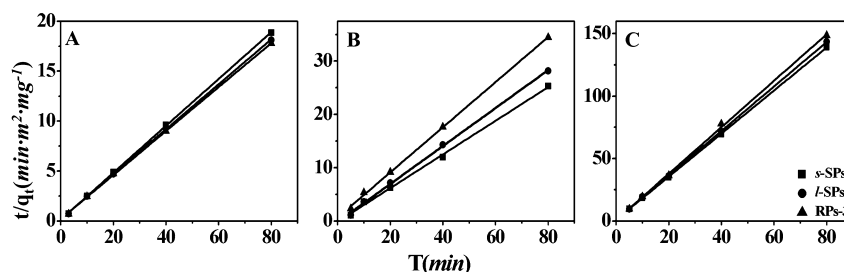

Figure 3. Pseudo-second-order kinetic plot fitting for the adsorption kinetic profile of (A) HSA, (B) HGG, (C) HSF onto different MSNs at 37 °C in pH 7.4 PBS.

Table 2. Adsorption Parameters of HSA, HGG, and HSF onto the Three Types of MSNs Obtained from Kinetic Pseudo-Second-Order Model

protein	materials	R^2	k_2 $(mg^{-1}\cdot m^2\cdot min^{-1})$	q_e $(mg\cdot m^{-2})$	h $(mg\cdot m^{-2}\cdot min^{-1})$
HSA	s-SPs	0.999	0.397	4.264	7.2250
	l-SPs	0.999	0.280	4.444	5.5340
	RPs-3	0.999	0.189	4.900	4.5455
HGG	s-SPs	0.998	0.957	3.207	9.8425
	l-SPs	0.999	1.176	2.845	9.5147
	RPs-3	0.999	0.278	2.362	1.549
HSF	s-SPs	0.999	3.164	0.5796	1.0628
	l-SPs	0.999	3.687	0.5615	1.1626
	RPs-3	0.999	5.732	0.5372	1.6545

The value of q_e and k_2 can be obtained from the slope and intercept of the plot of t/q_t against t, respectively, and the initial adsorption rate h was calculated from $k_2 q_e^2$.

The kinetic data for serum proteins adsorption onto different MSNs were plotted according to the pseudo-second-order kinetic model. As shown in Figure 3, the kinetics model yields a good agreement between the experimental (symbol) and simulated (line) data with residual square correlation coefficient ($R^2 > 0.997$). The rate parameters and saturated adsorption capacity were calculated and shown in Table 2. The measured adsorption q_t at time t was normalized by the surface area of each nanomaterial.

For HSA and HGG, the value of initial adsorption rate h onto the s-SPs, l-SPs, and RPs-3 decreased sequently because the pore expansion for l-SPs and the shape for RPs-3 make both of them have relatively low curvature in comparison with s-SPs. So, it is not difficult to conclude that the curvature of the three types of nanoparticles might be an important parameter mainly determining the adsorption rate of HSA and HGG. However, for HSF, its initial adsorption rate onto the s-SPs, l-SPs, and RPs-3 increased sequently. Because HSF is a rod-shaped protein, it should be adsorbed more easily onto rod-shaped

MSNs—RPs-3, corresponding to the most rapid adsorption rate, h. The saturated adsorption capacity, q_e, of HSA onto the s-SPs, l-SPs, and RPs-3 increased with the decrease of the curvature of the three MSNs, whereas the value of q_e for HGG and HSF decreased as the decrease of the curvature, which shows the similar tendency to the binding constant of protein-nanoparticles (Supporting Information, Figure S1 and Table S1). To further understand this phenomenon, we studied the conformational changes of adsorbed proteins onto the three types of nanomaterials.

Conformational changes of proteins usually happen upon their adsorption onto nanomaterials. We studied the MSNs-induced conformational changes of serum proteins after coincubating them with MSNs at 37 °C for 80 min by infrared spectroscopy. The results are summarized in Figures 4–6. Figure 4A shows the IR spectra of free HSA (a), and the complex of HSA−s-SPs (b), HSA−l-SPs (c), and HSA−RPs-3 (d) in the region of 1750−1475 cm^{-1}, which displays the amide I and amide II bands at 1653 and 1545 cm^{-1}, respectively. The amide I band is sensitive to the changes in the secondary structure and has therefore been widely used for studying protein conformation. The overall shape of the amide I band is
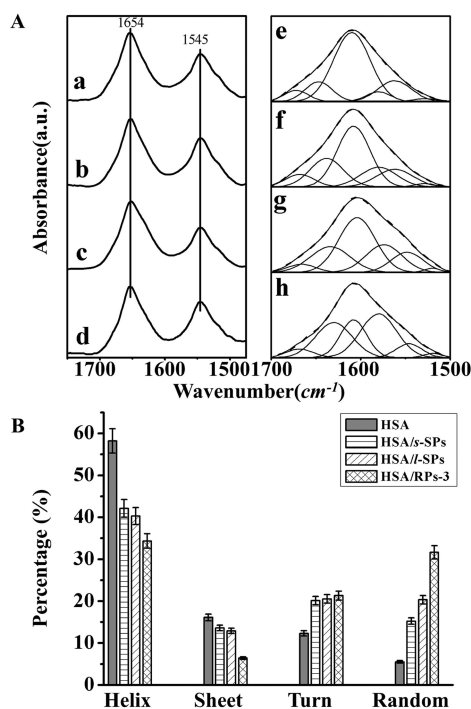
Figure 4. (A) FTIR adsorption spectra in the region of 1750−1475 cm^{-1} and curve-fitted spectra of the amide I band for free HSA (a, e), HSA absorbed onto s-SPs (b, f), l-SPs (c, g), and RPs-3 (d, h). (B) Fraction of the secondary structure of proteins as determined by quantitative curve-fitting analysis. The value was obtained from two or three experiments, and the error bars indicate standard deviations from the mean.

Figure 5. (A) FTIR adsorption spectra in the region of 1750−1475 cm^{-1} and curve-fitted spectra of the amide I band for free HGG (a, e), HGG absorbed onto s-SPs (b, f), l-SPs (c, g), and RPs-3 (d, h). (B) Fraction of the secondary structure of proteins as determined by quantitative curve-fitting analysis. The value was obtained from two or three experiments, and the error bars indicate standard deviations from the mean.

determined by the various secondary structure components of the proteins; therefore, the curve-fitting procedures with the second derivative resolution as a reference were used to determine the protein secondary structure. The band range 1610−1640 cm^{-1} was generally assigned to β-sheet, 1640−1650 cm^{-1} to random coil, 1650−1658 cm^{-1} to α-helix, 1660−1677 cm^{-1} to β-turn structure and 1680−1692 cm^{-1} to β-antiparallel.[30−32] The percentages of each secondary structure of HSA could be calculated based on the integrated areas of the component bands in the amide I band (Figure 4A(e−h)). To illustrate the change of each component bands clearly, the histogram and Table 3 were given to summarize the influence of the interaction between proteins and particles on the secondary structure of proteins (Figure 4B). As reported,[32] the free HSA had 58% α-helix, 17% β-sheet, 14% turn structure, 7% β-antiparallel, and 7% random coil (Figure 4B and Table 3). Upon interaction, there was a major decrease of α-helix from 58% (free HSA) to 42% (s-SPs), 40% (l-SPs) and 34% (RPs-3) with an increase in random coil from 7% (free HSA) to 15% (s-SPs), 20% (l-SPs), and 32% (RPs-3) and a reduction of β-sheet structure from 16% (free HSA) to 14% (s-SPs), 13% (l-SPs), and 6% (RPs-3) (Figure 4B). The major reduction of α-helix and increase of random coil might suggest a certain degree of protein unfolding. Obviously, the changes of the secondary structure of HSA were in turn increased when HSA was adsorbed onto the s-SPs, l-SPs, and RPs-3. This indicates that the interaction between HSA and RPs-3 whose curvature is the smallest, is the strongest. Such strong interaction might result in high saturated adsorption capacity and bigger binding coefficient.
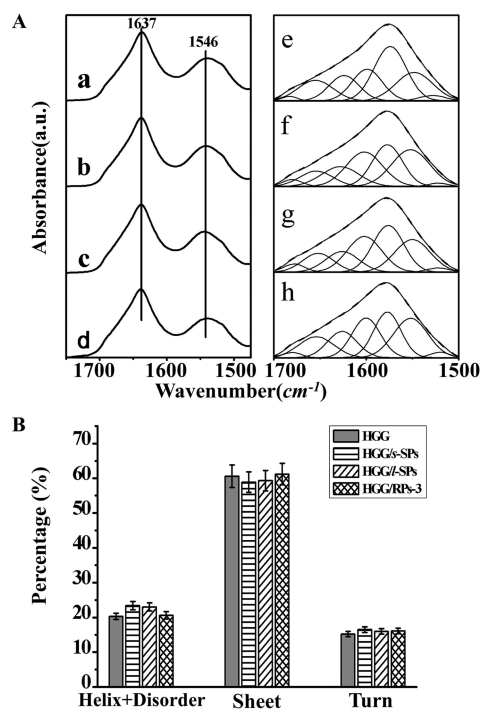
IR spectra obtained for free HGG and adsorbed HGG on the three types of particles show the maximum of the amide I band at ∼1637 cm^{-1} (Figure 5A(a−d)), which is typical for protein with high β-sheet content.[33,34] In Figure 5A(a−d), there are no apparent peak shifts for any spectrum of HGG. After Gaussian curve-fitting (Figure 5A(e−h)), the absorption peak centered at around 1650 cm^{-1} was attributed to the sum of α-helix and unordered structure, the peaks centered at 1675, 1636, and 1625 cm^{-1} were attributed to β-sheet, and the peaks at 1688 and 1661 cm^{-1} were assigned to β-turns. After calculation of the integrated areas of each component bands in the amide I band, it can be obtained that the free HGG has 61% β-sheet, 15% β-turns and 20% of the sum of α-helix and random coils[33] (Figure 5B and Table 4). Adsorption onto the s-SPs, l-SPs and RPs-3 did not cause significant disruption in the secondary structure. As many reports, the "hard" protein composed predominantly of β-sheet will keep the native conformation upon adsorption onto nanomaterials.[34−37] Without the effect of conformational changes, the saturated adsorption capacity and stability of adsorbed proteins onto the nanoparticles might be only determined by the property of nanomaterials. The q_e and binding constant decrease with the decrease of the curvature of manomaterials.

For HSF, we also analyzed the amide I band of free and adsorbed protein (Figure 5A(a−d)) by a Gaussian curve-fitting procedure. The feature band at around 1651−1655 cm^{-1} was assigned to α-helix, the peaks at 1616−1620, 1632−1639, and 1680−1689 cm^{-1} were assigned to β-sheet, the band at 1640−1650 cm^{-1} was assigned to random coils, and the peaks at 1668−1673 cm^{-1} were assigned to β-turn,[38,39] respectively (Figure 6A(e−h)). On the basis of the integrated areas of each
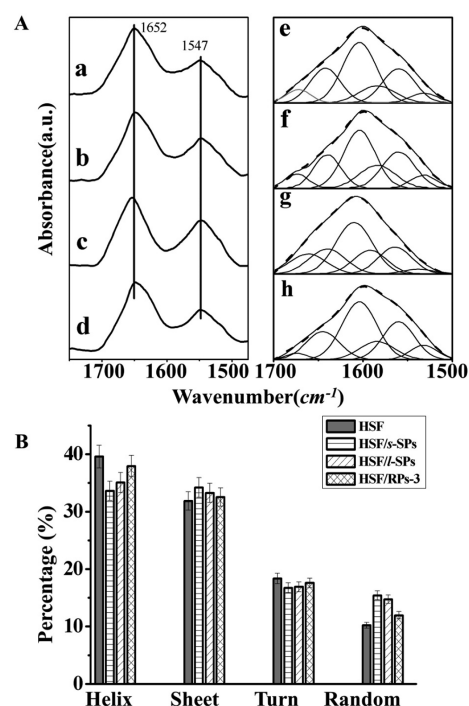
Figure 6. (A) FTIR adsorption spectra in the region of 1750−1475 cm^{-1} and curve-fitted spectra of the amide I band for free HSF (a, e), HSF absorbed onto s-SPs (b, f), l-SPs (c, g) and RPs-3 (d, h). (B) Fraction of the secondary structure of proteins as determined by quantitative curve-fitting analysis. The value was obtained from two or three experiments, and the error bars indicate standard deviations from the mean.

Table 3. Fraction of the Secondary Structure of HSA As Determined by Quantitative Curve-Fitting Analysis

		proportion (%)			
protein	secondary structure	free	s-SPs	l-SPs	RPs-3
HSA	α-helix	58 ± 3	42 ± 2	40 ± 2	34 ± 2
	β-sheet	16 ± 1	14 ± 2	13 ± 2	6 ± 2
	β-turn	12 ± 1	20 ± 1	20.5 ± 1	21 ± 1
	random	6 ± 1	15 ± 1	20 ± 1	32 ± 1

Table 4. Fraction of the Secondary Structure of HGG As Determined by Quantitative Curve-Fitting Analysis

		proportion (%)			
protein	secondary structure	free	s-SPs	l-SPs	RPs-3
HGG	α-helix + random	20 ± 1	23 ± 1	23 ± 1	21 ± 1
	β-sheet	61 ± 3	59 ± 3	59 ± 3	61 ± 3
	β-turn	15 ± 1	16.5 ± 1	16 ± 1	16 ± 1

component, we can obtain that free HSF has 40% α-helix, 32% β-sheet, 18% β-turn, and 10% random coil[38] (Figure 6B and Table 5). Upon adsorption, there is an obvious decrease of α-helix from 40% (free HSF) to 34% (s-SPs), 35% (l-SPs), and 38% (RPs-3) with an increase in random coil from 10% (free HSF) to 15% (s-SPs), 15% (l-SPs), and 12% (RPs-3) (Figure 6B). It seems that HSF, with a rod-like structure, could more easily adhere to a relatively flat surface and maintain its native structure. Correspondingly, conformational changes after interaction with RPs-3 was not as significant as that of adsorbed onto the s-SPs and l-SPs (Figure 6B and Table 5). The minor reduction of α-helix and the increase of random coil

Table 5. Fraction of the Secondary Structure of HSF As Determined by Quantitative Curve-Fitting Analysis

		proportion (%)			
protein	secondary structure	free	s-SPs	l-SPs	RPs-3
HSF	α-helix	40 ± 2	34 ± 1	35 ± 1	38 ± 2
	β-sheet	32 ± 2	34 ± 2	33 ± 2	32.5 ± 2
	β-turn	18 ± 1	16 ± 1	17 ± 1	18 ± 1
	random	10 ± 1	15 ± 1	14 ± 1	12 ± 1

might suggestion a partial protein destabilization. s-SPs and l-SPs could induce HSF bending to adjust the surface with a certain curvature, along with some secondary structure destabilization and the increase of q_e and binding constant.

Effect of Shape and Pore Size of MSNs on Interaction between Particles and RBCs. The impact of pore size and geometry of MSNs on RBCs was evaluated by a hemolysis assay. The hemolytic kinetics was evaluated by exposing the RBCs to each sample at a concentration of 500 μg/mL for 10, 24, 40, 60, and 80 min each at 37 °C (Figure 7A). The photographs of RBCs after exposure to the three types of MSNs for different time periods were shown in Figure 7B. As shown in Figure 7A,B, the hemolysis percentage of RBCs increases in a time-dependent manner for the three types of MSNs. Hemolysis of RBCs incubated with the l-SPs is more serious than the s-SPs, indicating that the enlarged pore size increases the hemolytic activity of MSNs. Furthermore, geometry is another important factor that affects hemolysis. The RPs-3 with aspect ratios of ∼3 displays more apparently hemolytic activity than the two spherical nanoparticles (Figure 7A,B). Because the surface curvature of the s-SPs, l-SPs, and RPs-3 decreases sequently, our results indicate that the hemolytic activity of MSNs is also surface-curvature-dependent. A decrease of the surface curvature results in an increasing of hemolytic activity of MSNs. This might have a relationship with the curvature-dependent structural changes of some biomolecules. As our discussion above, lower curvature of MSNs results in more apparently conformational changes of some proteins. Interaction between MSNs with lower curvature and RBCs might induce significant structural changes of some proteins on RBCs membranes, which might accelerate the hemolysis of RBCs. In the report of Lin et al.,[18] with the similar particles diameters, MSNs displayed lower hemolytic activity than nonporous particles. Whereas, the data in the work of Yu et al.[17] revealed that MSNs induced higher hemolysis than stöber nanoparticles, which was completely opposite to the result of Lin et al. Meanwhile, we find that the MSNs in the work of Lin et al. have smaller pore size than the MSNs used in Yu et al.'s work. Therefore, we speculate that the difference between the two opposite results might come from the variation of pore scales, although Yu et al. have given the reasonable explanation about the hemolysis difference between MSNs and nonporous particles based on the difference in the zeta potentials of the two particles. To clarify this point, we additionally synthesized two types of stöber nanoparticles with the same diameter (60 nm) but different zeta potentials (more negative particles SS-m and less negative particles SS-l, see Figure S2 (Supporting Information)) and studied their hemolytic activities. It was found that the hemolytic activity of SS-l was slightly higher than SS-m. The result indicates that the increase of the zeta potential will increase the hemolytic activity of the materials as Yu et al.'s report. Meanwhile, we found that at 80 min, the hemolysis was sequently increased in the order of SS-l, s-SPs, and l-SPs. The
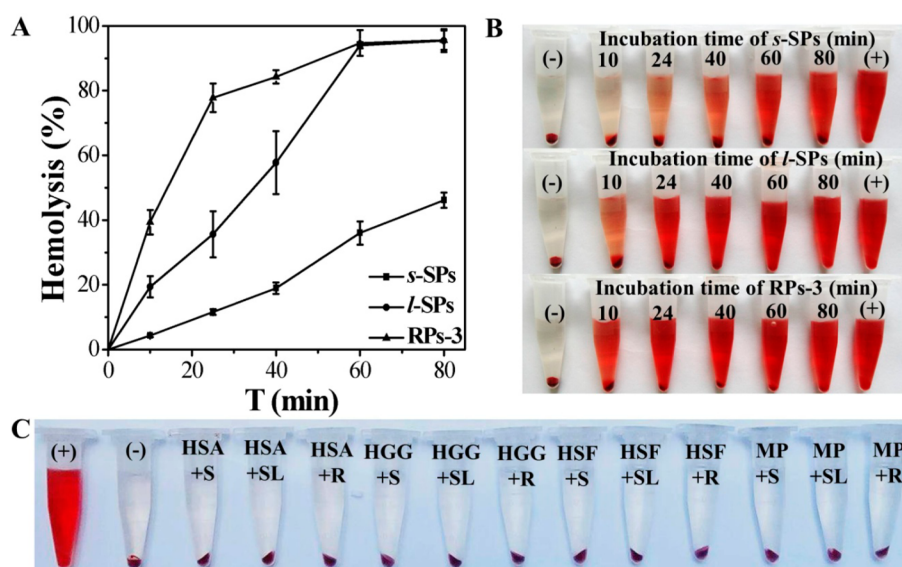
Figure 7. (A) Hemolysis percentage of human RBCs upon incubation with different MSNs at a concentration of 500 μg/mL, plotted as a function of time. The value was obtained from two or three experiments, and the error bars indicate standard deviations from the mean. (B) Photographs of RBCs after exposure to different types of MSNs at a concentration of 500 μg/mL for different times. (C) Photographs of RBCs hemolysis assay after RBCs were mixed with either separated protein (HSA, HGG, and HSF) or mixed proteins (MPs) and three types of MSNs. In these experiments, D.I. water (+) and PBS (−) were used as positive and negative control, respectively.

pore sizes of the three types of nanoparticles are 0, 2.2, and 3.0 nm, respectively, and these three particles have the similar zeta potentials (−12.9, −7.6, and −7.7 mV) and average hydrodynamic sizes (Supporting Information, Table S2). These further eliminate the effects of zeta potential and aggregation of silica nanoparticles on hemolysis of RBCs.[40] Therefore, we deduce that the hemolytic activity of MSNs is pore size-dependent. Yu et al. also reported that MSNs with aspect ratio of 2 caused more apparent hemolysis than spherical particles.[19] However, the ones with an aspect ratio of 4 and 8 displayed lower hemolysis than the MSNs with an aspect ratio of 2. Combining with our results, we speculate that there may possibly be a "threshold" for the surface curvature to influence the hemolytic activity of MSNs. To further identify the possibility, we synthesized one more type of MSNs whose aspect ratio was about 10 (RPs-10) and investigated its hemolytic activity (Supporting Information, Figure S3). Instead, we found that the hemolytic activity of RPs-10 was lower than that of RPs with an aspect ratio of 3. However, we still cannot point out the "threshold" at the moment due to the limit data. It will be the purpose of our future work.

From the study of adsorption kinetics of the proteins onto MSNs and hemolysis kinetics of RBCs induced by MSNs, it is not difficult to find that the affinity of serum proteins onto MSNs was stronger than that of RBCs. Adsorption of serum proteins onto MSNs gets to equilibrium in nearly 5 min at 37 °C in PBS (pH 7.4) (Figure 2) when hemolysis of RBCs just reaches merely ∼10% (Figure 7A). Therefore, it is necessary to evaluate the hemolytic activity of MSNs in the presence of serum proteins. The three types of MSNs were added respectively into the mixture of RBCs with either separated HSA, HGG, HSF, or their mixture at 37 °C. After incubation for 3 h (Figure 7C), no hemolysis was observed at any condition (Figure 7C). Because the proteins have higher affinity for MSNs than RBCs, after adding MSNs into the mixture of RBCs with proteins, proteins will be adsorbed onto the surface of MSNs first. The resulting protein corona

obviously prevents RBC hemolysis. According to our results, it is not difficult to obtain the conclusion that serum proteins play an important role and should not be ignored when we inspect the biological behavior of intravenously injected nanoparticles.

4. CONCLUSIONS

Here we have described the effects of pore scale and morphology of MSNs on their interaction with serum proteins and RBCs. It was shown that the initial adsorption rate h for HSA and HGG onto the s-SPs, l-SPs, and RPs-3 decreased sequently as the surface curvature decreased. However, the initial adsorption rate for HSF increased with decreased curvature due to the rod-shaped property of HSF. The changes of the secondary structure of HSA were, in turn, increased when HSA was adsorbed onto the s-SPs, l-SPs, and RPs-3, which also enhanced the saturated adsorption capacity and binding stability of HSA onto the MSNs. As a rigid protein, adsorption of HGG onto the s-SPs, l-SPs, and RPs-3 did not cause significant disruption in the secondary structure of HGG. Adsorbed HSF onto the surface of s-SPs and l-SPs was bended to adjust the surface curvature of MSNs, which resulted in the loss of some secondary structure and the increase of the saturated adsorption capacity and binding constant. The surface curvature of the s-SPs, l-SPs, and RPs-3 also determined their cytotoxicity to RBCs. However, their cytotoxicity was completely reduced in the presence of serum proteins.

■ ASSOCIATED CONTENT

⑤ Supporting Information

Preparation of Stöber silica (SS-m and SS-l) nanoparticles (NPs), preparation of RPs-10, calculating binding constants of protein-nanoparticles, Langmuir adsorption equation plot fitting, kinetic parameters of the adsorption of HSA, HGG and HSF, transmission electron microscopy image of SS-l, plot of hemolysis percentage of human RBCs upon incubation with s-SPs, l-SPs, SS-m, and SS-l, transmission electron microscopy image of RPs-10, and plot of hemolysis percentage of human

RBCs upon incubation with s-SPs, l-SPs, RPs-3, and RPs-10. This material is available free of charge via the Internet at http://pubs.acs.org.

■ AUTHOR INFORMATION

Corresponding Author

*Xiue Jiang, Professor, PhD. Phone: +86 431 85262426. Fax: +86 431 85685653. E-mail: jiangxiue@ciac.ac.cn.

Notes

The authors declare no competing financial interest.

■ REFERENCES

(1) Cedervall, T.; Lynch, I.; Lindman, S.; Berggård, T.; Thulin, E.; Nilsson, H.; Dawson, K. A.; Linse, S. *Proc. Natl. Acad. Sci. U. S. A.* **2007**, *104*, 2050−2055.

(2) Hulander, M.; Lundgren, A.; Berglin, M.; Ohrlander, M.; Lausmaa, J.; Elwing, H. *Int. J. Nanomed.* **2011**, *6*, 2653−2666.

(3) Göppert, T. M.; Müller, R. H. *J. Drug. Targeting* **2005**, *13*, 179−187.

(4) Lartigue, L.; Wilhelm, C.; Servais, J.; Factor, C.; Dencausse, A.; Bacri, J.-C.; Luciani, N.; Gazeau, F. *ACS Nano* **2012**, *6*, 2665−2678.

(5) Zook, J. M.; MacCuspie, R. I.; Locascio, L. E.; Halter, M. D.; Elliott, J. T. *Nanotoxicology* **2011**, *5*, 517−530.

(6) Saxena, V.; Diaz, A.; Clearfield, A.; Batteas, J. D.; Hussain, M. D. *Nanoscale* **2013**, *5*, 2328−2336.

(7) Chen, L.; Kang, B.; Ling, J. *J. Nanopart. Res.* **2013**, *15*, 1−9.

(8) Zook, J.; Halter, M.; Cleveland, D.; Long, S. *J. Nanopart. Res.* **2012**, *14*, 1−9.

(9) Chambers, E.; Mitragotri, S. *Exp. Biol. Med. (London, U. K.)* **2007**, *232*, 958−966.

(10) Yoo, J.-W.; Chambers, E.; Mitragotri, S. *Curr. Pharm. Des.* **2010**, *16*, 2298−2307.

(11) Trewyn, B. G.; Giri, S.; Slowing, I. I.; Lin, V. S. Y. *Chem. Commun.* **2007**, 3236−3245.

(12) Liong, M.; Lu, J.; Kovochich, M.; Xia, T.; Ruehm, S. G.; Nel, A. E.; Tamanoi, F.; Zink, J. I. *ACS Nano* **2008**, *2*, 889−896.

(13) Vivero-Escoto, J. L.; Slowing, I. I.; Trewyn, B. G.; Lin, V. S. Y. *Small* **2010**, *6*, 1952−1967.

(14) Tsai, C.-P.; Chen, C.-Y.; Hung, Y.; Chang, F.-H.; Mou, C.-Y. *J. Mater. Chem.* **2009**, *19*, 5737−5743.

(15) Cheng, S.-H.; Lee, C.-H.; Chen, M.-C.; Souris, J. S.; Tseng, F.-G.; Yang, C.-S.; Mou, C.-Y.; Chen, C.-T.; Lo, L.-W. *J. Mater. Chem.* **2010**, *20*, 6149−6157.

(16) Zhao, Y.; Sun, X.; Zhang, G.; Trewyn, B. G.; Slowing, I. I.; Lin, V. S. Y. *ACS Nano* **2011**, *5*, 1366−1375.

(17) Yu, T.; Malugin, A.; Ghandehari, H. *ACS Nano* **2011**, *5*, 5717−5728.

(18) Lin, Y.-S.; Haynes, C. L. *J. Am. Chem. Soc.* **2010**, *132*, 4834−4842.

(19) Slowing, I. I.; Wu, C.-W.; Vivero-Escoto, J. L.; Lin, V. S. Y. *Small* **2009**, *5*, 57−62.

(20) Joglekar, M.; Roggers, R. A.; Zhao, Y.-N; Trewyn, Brian G. *RSC Adv.* **2013**, *3*, 2454−2461.

(21) He, Q.-J; Zhang, J.-M; Shi, J.-L; Zhu, Z.-Y; Zhang, L.-X; Bu, W.-B; Guo, L.-M; Chen, Y. *Biomaterials* **2010**, *31*, 1085−1092.

(22) Yildirim, A.; Ozgur, E.; Bayindir, M. *J. Mater. Chem. B* **2013**, *1*, 1909−1920.

(23) Lesniak, A.; Fenaroli, F.; Monopoli, M. R.; Aberg, C.; Dawson, K. A.; Salvati, A. *Acs Nano* **2012**, *6*, 5845−5857.

(24) Ge, C.; Du, J.; Zhao, L.; Wang, L.; Liu, Y.; Li, D.; Yang, Y.; Zhou, R.; Zhao, Y.; Chai, Z.; Chen, C. *Proc. Natl. Acad. Sci. U. S. A.* **2011**, *108*, 16968−16973.

(25) Shi, J.; Hedberg, Y.; Lundin, M.; Odnevall Wallinder, I.; Karlsson, H. L.; Möller, L. *Acta Biomater.* **2012**, *8*, 3478−3490.

(26) Yu, T.; Greish, K.; McGill, L. D.; Ray, A.; Ghandehari, H. *ACS Nano* **2012**, *6*, 2289−2301.

(27) Mizutani, M.; Yamada, Y.; Nakamura, T.; Yano, K. *Chem. Mater.* **2008**, *20*, 4777−4782.

(28) Mizutani, M.; Yamada, Y.; Yano, K. *Chem. Commun.* **2007**, 1172−1174.

(29) Ho, Y. S.; McKay, G. *Process Saf. Environ. Prot.* **1998**, *76B*, 332−340.

(30) Roach, P.; Farrar, D.; Perry, C. C. *J. Am. Chem. Soc.* **2006**, *128*, 3939−3945.

(31) Schwinté, P.; Ball, V.; Szalontai, B.; Haikel, Y.; Voegel, J. C.; Schaaf, P. *Biomacromolecules* **2002**, *3*, 1135−1143.

(32) Charbonneau, D.; Beauregard, M.; Tajmir-Riahi, H.-A. *J. Phys. Chem. B* **2009**, *113*, 1777−1784.

(33) Byler, D. M.; Susi, H. *Biopolymers* **1986**, *25*, 469−487.

(34) Giacomelli, C. E.; Bremer, M. G. E. G.; Norde, W. *J. Colloid Interface Sci.* **1999**, *220*, 13−23.

(35) Vermeer, A. W. P.; Norde, W. *J. Colloid Interface Sci.* **2000**, *225*, 394−397.

(36) Bee, J. S.; Chiu, D.; Sawicki, S.; Stevenson, J. L.; Chatterjee, K.; Freund, E.; Carpenter, J. F.; Randolph, T. W. *J. Pharm. Sci.* **2009**, *98*, 3218−3238.

(37) Bee, J. S.; Davis, M.; Freund, E.; Carpenter, J. F.; Randolph, T. W. *Biotechnol. Bioeng.* **2010**, *105*, 121−129.

(38) Schwinté, P.; Voegel, J. C.; Picart, C.; Haikel, Y.; Schaaf, P.; Szalontai, B. *J. Phys. Chem. B* **2001**, *105*, 11906−11916.

(39) van Stokkum, I. H. M.; Linsdell, H.; Hadden, J. M.; Haris, P. I.; Chapman, D.; Bloemendal, M. *Biochemistry* **1995**, *34*, 10508−10518.

(40) Thomassen, L. C. J.; Rabolli, V.; Masschaele, K.; Alberto, G.; Tomatis, M.; Ghiazza, M.; Turci, F.; Breynaert, E.; Martra, G.; Kirschhock, C. E. A.; Martens, J. A.; Lison, D.; Fubini, B. *Chem. Res. Toxicol.* **2011**, *24*, 1869−1875.